Engineering the Li Storage Properties of Graphene Anodes: Defect Evolution and Pore Structure Regulation

Zhuzhu Du,[†] Wei Ai,[†,‡] Chencheng Sun,[†] Chenji Zou,[‡] Jianfeng Zhao,[†] Yu Chen,[‡] Xiaochen Dong,[†] Juqing Liu,*[,†] Gengzhi Sun,[†] Ting Yu,*[,‡] and Wei Huang*[,†,§]

[†]Key Laboratory of Flexible Electronics (KLOFE) & Institute of Advanced Materials (IAM), National Jiangsu Synergetic Innovation Center for Advanced Materials (SICAM), Nanjing Tech University (NanjingTech), 30 South Puzhu Road, Nanjing 211816, China

[‡]Division of Physics and Applied Physics, School of Physical and Mathematical Sciences, Nanyang Technological University, 637371, Singapore

[§]Key Laboratory for Organic Electronics & Information Displays (KLOEID) and Institute of Advanced Materials (IAM), Nanjing University of Posts & Telecommunications, Nanjing 210023, Jiangsu China

S *Supporting Information*
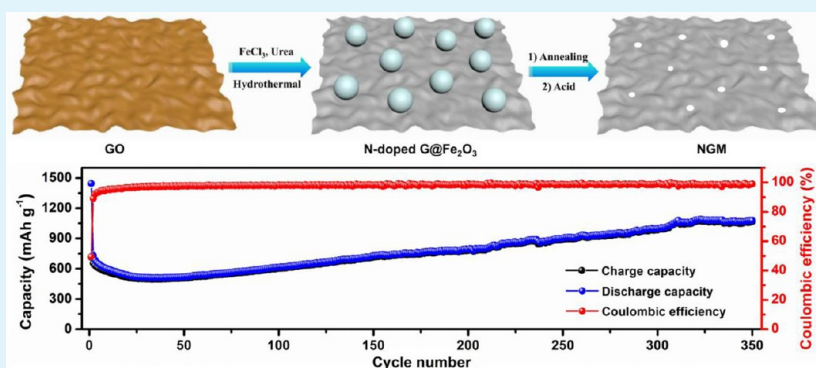
ABSTRACT: A general and mild strategy for fabricating defect-enriched graphene mesh (GM) and its application toward the anode of Li-ion batteries (LIBs) has been reported. The GM with a pore size of 60−200 nm is achieved by employing Fe_2O_3 as the etching reagent that is capable of locally etching the graphene basal plane in a relatively mild manner. Upon different drying technologies, that is, oven drying and freeze-drying, GMs with different porous structure are obtained. The electrochemical Li storage properties of GMs in comparison with graphene aerogels (GAs) disclose that both defect sites and porous structure are crucial for the final anodic performances. We show that only when merged with rich porosity, the GM anode can achieve a better Li storage performance than that of GA. Moreover, we further fabricated nitrogen-doped GM (NGM) using urea as the nitrogen source with a freeze-drying process. Benefiting from the unique structural characteristics, that is, plentiful defects, abundant pores, and nitrogen doping, the NGM anode exhibits high Li storage capacity with good cyclic stability (1078 mAh g^{-1} even after 350 continuous cycles at a current density of 0.2 C) and outstanding rate capability. Our finding provides fundamental insights into the influence of defects and pore structure on the Li storage properties of graphene, which might be helpful for designing advanced graphene-based anodes for LIBs.

KEYWORDS: graphene mesh, Li-ion batteries, pore structure, N doping, general strategy

◾ INTRODUCTION

Because of their unique physicochemical properties, graphene-based materials have been attracting great research interests as one class of the most promising alternative candidates to current commercial graphite-based anodes for next generation Li-ion batteries (LIBs) with higher energy storage capability.[1,2] The fascinating two-dimensional morphology of graphene endows the adsorption of Li on both sides of the sheet, leading to a double Li storage capacity of 744 mAh g^{-1} with respect to its graphite counterpart.[3,4] Unfortunately, the preparation of graphene-based anodes inevitably faces the problem of aggregation arising from the strong intramolecular

interactions (e.g., $\pi-\pi$ stacking and van der Waals interaction) between the graphene sheets, which substantially blocks the electroactive sites for Li storage, and simultaneously, harmful for mass transport and electrolyte penetration.[5,6] To this end, intensive efforts have been devoted to fabricating porous graphene anodes with rich porosity.[7−9] The abundant pores in the electrode materials not only function as efficient reservoirs for Li storage but also ensure high electrolyte accessibility.
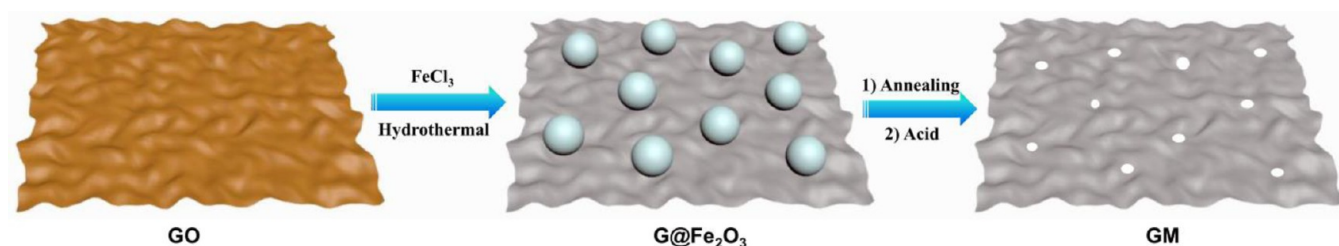
Figure 1. Schematic diagrams of the preparation of GM. The G@Fe$_2$O$_3$ was synthesized by a hydrothermal process using GO and FeCl$_3$ as precursors with the assistance of anionic SDS surfactant. The resulting Fe$_2$O$_3$ anchored graphene underwent annealing at 850 °C for 2 h and then exposed to a dilute HCl etching solution to achieve GM.

However, the low Li ions diffusivity in graphene, especially along the cross-plane, makes sluggish kinetics for Li ions diffusion in the electrode.[10,11] As a consequence, the lithiation and delithiation in graphene-based anodes are restricted to occur only at the edge regions, which severely limits their electrochemical performances.

To address this problem, one effective strategy is to introduce in-plane pores into the graphene layer so as to speed up Li ions diffusion throughout the whole electrode. In this regard, graphene mesh (GM), also known as holey graphene that possesses a certain number of nanoscale pores/holes in the basal plane of graphene sheet, has been proposed.[12,13] Such an appealing architecture is capable of providing fast diffusion channels for Li ions, and more importantly, guarantees high Li storage capacity by virtue of the as-formed defects and edge-type sites for further Li accommodation.[14,15] So far, the preparation of GM for LIBs anode application has been reported by means of diverse techniques, such as template-assisted chemical vapor deposition (e.g., porous MgO and expanded vermiculite),[16,17] chemical etching (e.g., KOH, H$_2$O$_2$, HNO$_3$, and NaI),[18−21] metal etching (e.g., Ni, Fe, Cu, and Co)[22,23] and air oxidation.[24] Among them, the metal etching method developed by Liu et al.[22] allows for the scalable production of GM in a very efficient route since it does not involve corrosive/hazardous chemicals (e.g., H$_2$ and KOH), and the graphene oxide (GO) precursor can now be easily obtained via the mature oxidation-exfoliation technology.[25] However, the etching process by metal nanoparticles, for example, Fe, is so violent that the graphene sheets turn into small pieces, which is not beneficial for electrochemical applications. Therefore, facile and mild approaches for mass production of GM are still lacking.

In this work, we report a facile and efficient strategy to prepare GM without the formation of tattered structures by employing Fe$_2$O$_3$ as a mild etching reagent. The fabrication procedure first involves a hydrothermal reaction to construct Fe$_2$O$_3$ decorated graphene composite (G@Fe$_2$O$_3$), which subsequently experiences an annealing process to achieve GM. During thermal treatment, the Fe$_2$O$_3$ nanoparticles could locally etch the graphene basal plane to form a defect-enriched holey structure. The Li storage properties of GM in comparison with graphene aerogel (GA) are comprehensively investigated. In addition, the pore structure regulation on the influence of the final electrochemical performance of GA and GM is explored as well. We show that improved Li storage performances in GM can only be realized when it is merged with a moderate porous structure, which is advantage for the accessibility of electrolyte. To further upgrade its performance, we also fabricated a nitrogen doped GM (NGM) by using urea as the nitrogen source. The exquisite structure, that is, plentiful

defects and unique porous architecture, combined with the nitrogen doping, leads to exceptional anodic performances in terms of high specific capacity with long cyclic life and superb rate capability.

EXPERIMENTAL SECTION

Preparation of GO. Graphite was used as received from Qingdao Black Dragon Graphite Co., Ltd. The oxidation of graphite was carried out by a modified Hummers' method following our previously reported procedures.[26] The resultant product was purified by dialysis and subsequently dried by a freeze-dryer.

Preparation of Oven-Dried Graphene Mesh (O_GM). Two milligrams of sodium dodecyl sulfate (SDS) was dissolved in 40 mL of GO aqueous solution (3 mg mL^{-1}) under sonication. With constant stirring, 160 mg of FeCl$_3$ was added into the solution. Subsequently, the mixture was transferred into a Teflon-lined autoclave (50 mL) for hydrothermal reaction (180 °C for 12 h). The as-formed gel-like product was rinsed with deionized water for three times prior to be dried in a 100 °C electric oven. After that, the sample was calcined in a tube furnace at 850 °C for 2 h (heating rate: 5 °C min^{-1}) under Ar atmosphere (flow rate: 100 sccm). Finally, the resultant powder was etched with 8 M of HCl aqueous solution, collected by vacuum filtration, and then washed with deionized water until the PH value is 7 before drying in the oven.

Preparation of Freeze-Dried Graphene Mesh (F_GM). F_GM was prepared under the same experimental parameters as O_GM except all the drying processes were conducted in a freeze-dryer.

Preparation of NGM. NGM was prepared similar to F_GM except that 360 mg of urea was added into the SDS and GO mixture.

Preparation of Graphene Aerogels. Forty milliliters of GO aqueous solution (3 mg mL^{-1}) was subjected to hydrothermal treatment at 180 °C for 12 h. Then the oven-dried graphene aerogel (O_GA) or freeze-dried graphene aerogel (F_GA) was calcined at 850 °C for 2 h in Ar atmosphere.

Characterization. Morphological characterizations of the samples were conducted using a Zeiss Dual Beam FIB/SEM instrument, JEOL JSM-6700F electron microscope and JEOL JEM-2010 high resolution transmission electron microscope. Structural characterizations of the products were carried out on a Bruker D8 diffractometer, PerkinElmer PHI 5600 XPS system, Micromeritics model ASAP 2020 instrument and WITEC CRM200 Raman system.

Electrochemical Characterizations. The Li storage properties of the samples were tested on a NEWARE 8-channel battery testing system using coin-type cells. The working electrodes were obtained by coating N-methyl-2-pyrrolidone (NMP) based slurries onto 10 μm thick copper foils. Typically, the slurries were fabricated by mixing 80 wt % of electrode material, 10 wt % of acetylene black and 10 wt % of polyvinylidene fluoride in NMP with constant stirring. The active materials coated copper foils were dried in a vacuum oven at 100 °C overnight. Subsequently, 1.2 cm diameter circular electrodes were punched out, weighed and assembled in a pure Ar filled glovebox with pure Li foil and 1 M LiPF$_6$ in ethylene carbonate/ethyl methyl carbonate/dimethyl carbonate (1:1:1, vol %) as the counter electrode and electrolyte, respectively. For a single electrode, the loading amount of active materials was controlled to be 1.5−1.9 mg. All cells were
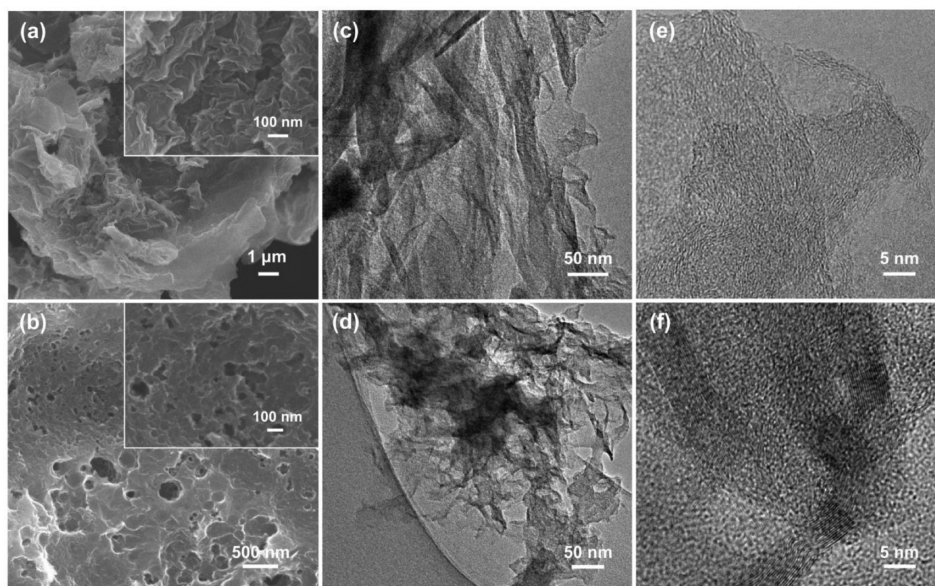
Figure 2. Morphological characterizations. FESEM images of (a) O_GA and (b) O_GM. Inset: Corresponding higher-magnification FESEM images. TEM images of (c) O_GA and (d) O_GM. HRTEM images of (e) O_GA and (f) O_GM.
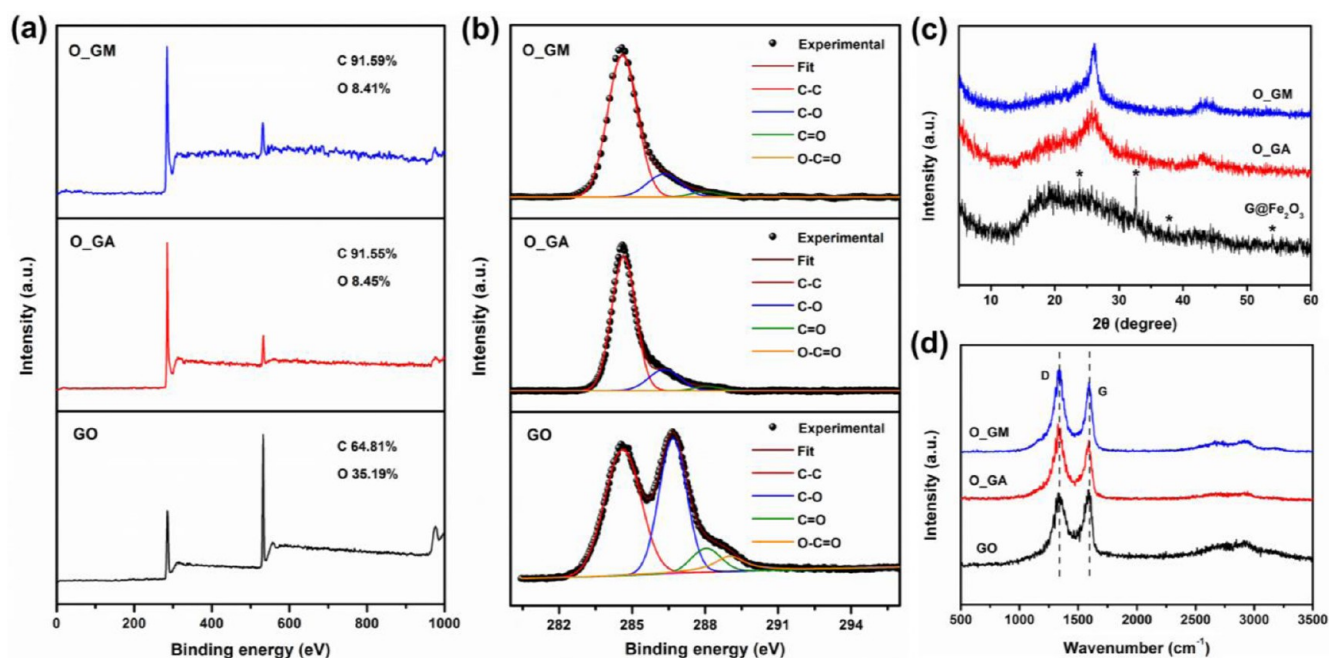

Figure 3. Structural characterizations. (a) XPS survey spectra and (b) high-resolution C 1s XPS spectra of GO, O_GA and O_GM. (c) XRD patterns of G@Fe$_2$O$_3$, O_GA and O_GM. (d) Raman spectra of GO, O_GA and O_GM.

tested in the voltage range between 0.005 and 3.0 V (vs Li/Li$^+$), and the specific capacities were all calculated according to the mass of active materials.

■ RESULTS AND DISCUSSION

The synthetic procedure of GMs is schematically illustrated in Figure 1. First, G@Fe$_2$O$_3$ was prepared by a simple hydrothermal reaction between FeCl$_3$ and GO with the help of SDS. Field-emission scanning electron microscopy (FESEM) images reveal that the Fe$_2$O$_3$ nanoparticles with a uniform size of ∼100 nm were densely deposited on the graphene sheets, forming fold and wrinkle structures (Figure S1). Subsequently, the G@Fe$_2$O$_3$ was calcined at 850 °C under Ar atmosphere,

during which the Fe$_2$O$_3$ particles can locally etch the surrounded graphene sheets to form a holey structure.[27] Finally, the Fe$_2$O$_3$ was removed by HCl aqueous solution to obtain GMs. For comparison, GAs were also prepared under the conditions similar to GMs (see Experimental Section for details).

The morphologies of O_GM and O_GA were examined by FESEM and transmission electron microscopy (TEM). As shown in the FESEM images in Figure 2a, O_GA shows a stacked morphology with curved graphene at the surface and edges. On clear contrast, O_GM consists of numerous in-plane pores on the bulk graphene monoliths, indicating the successful introduction of holey structures (Figure 2b). The pores are

found to be nonuniformly distributed on the bulk structure and their sizes are in the range of a few nanometers to hundreds of nanometers, which are presumably caused by the loose of Fe_2O_3 nanoparticles during etching. TEM images (Figure 2c and 2d) suggest that O_GA is composed of thick graphene sheets that form a graphite-like structure, whereas O_GM displays an aggregated structure constructed by etched graphene sheets with in-plane pores. The high-resolution TEM (HRTEM) images of both O_GM and O_GA (Figure 2e and 2f) illustrate discontinuous lattice structures, implying the existence of defects and remaining oxygen-containing functional groups on graphene sheets that are induced by oxidation.[28,29] It is worth mentioning that such structural damages are beneficial for electrochemical reactions.

X-ray photoelectron spectroscopy (XPS) measurements were used to probe the elemental composition of the samples. The XPS survey scans (Figure 3a) display two peaks located at ~285.6 and ~531.8 eV, assignable to the C 1s and O 1s, respectively.[15,30] The C/O ratios are calculated to be 10.9 for O_GM and 10.8 for O_GA, which are significantly larger than that of GO (1.84), verifying the effective removal of oxygen-containing functional groups. The four deconvoluted peaks in the high-resolution C 1s XPS spectrum of GO (Figure 3b) suggest the presence of four types of carbon bonds, that is, C−C at 284.6 eV, C−O at 286.7 eV, C=O at 288.0 eV, and O−C=O at 289.0 eV.[31,32] However, the intensities of these functional groups are substantially decreased or even disappeared in the C 1s XPS spectra of O_GM and O_GA, once again demonstrating the sufficient reduction of GO after hydrothermal and annealing treatments. Figure 3c exhibits the X-ray diffraction (XRD) patterns of $G@Fe_2O_3$, O_GM and O_GA. $G@Fe_2O_3$ presents a hump-shaped peak at $2\theta = 13-33°$ with four diffraction peaks at $2\theta = 23.9°, 32.6°, 37.7°$ and $53.9°$. The former broad peak is assigned to the (002) plane of graphite, and the other peaks can be successively ascribed to the (210), (300), (320) and (422) planes of γ-Fe_2O_3 (maghemite, JCPDS No. 04−0755).[33,34] For O_GM and O_GA, the 002 peak stemming from the restacking of graphene sheets shifts to ~26.1°, indicating the reduction of GO associated with its aggregation.[35,36] This is further confirmed by Raman spectroscopy (Figure 3d), which displays increased I_D/I_G ratios in O_GM (1.05) and O_GA (1.06) compared with GO (0.98).

Nitrogen adsorption−desorption characterizations were used to examine the porous texture of the samples. Figure 4a shows the N_2 adsorption−desorption isotherms of O_GM and O_GA, both of which exhibit a type IV pattern with apparent hysteresis loops, indicating the existence of mesopores within these two samples.[9,37] The Brunauer−Emmett−Teller (BET) surface area of O_GM and O_GA is determined to be 138 and 104 m^2 g^{-1}, respectively, consistent with the previously reported common GAs.[38] The slightly larger surface area of O_GM with respect to O_GA probably arises from the presence of in-plane pores that could alleviate the restacking/aggregation of graphene sheets to some extent. The corresponding pore size distribution curves of O_GM and O_GA (Figure 4b) show a wide pore size distribution ranging from 2 to 200 nm. The pore structure parameters summarized in Table 1 reveal that O_GM and O_GA have almost the same total pore volume and average pore diameter, which could be attributed to the collapse of pores within the graphene sheets during oven drying, agreeing well with the morphological characterizations shown in Figure 2.
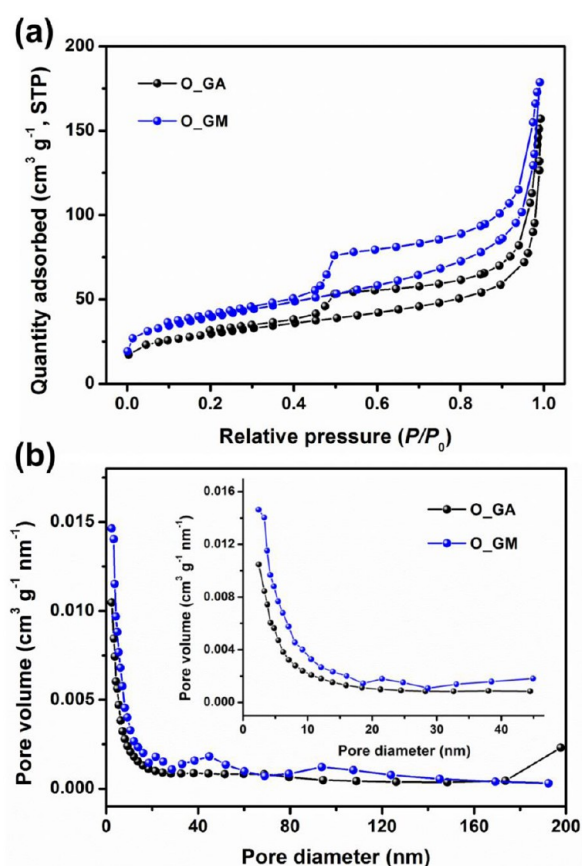

Figure 4. (a) N_2 adsorption−desorption isotherms and (b) the corresponding pore size distribution curves (inset shows magnified 0−45 nm region) of O_GA and O_GM.

Table 1. Pore Structure Parameters of O_GA, O_GM, F_GA, F_GM, and NGM

sample	BET surface area (m^2 g^{-1})	total pore volume (cm^3 g^{-1})	average pore diameter (nm)
O_GA	104	0.21	8.20
O_GM	138	0.27	7.94
F_GA	311	0.32	4.17
F_GM	381	0.29	3.06
NGM	487	0.86	7.09

The electrochemical Li storage performances of O_GM and O_GA were studied using coin-type half cells (CR2032). Cyclic voltammetry (CV) was first conducted in a voltage ranges from 0.005 to 3 V to evaluate the electrochemical behaviors of the electrodes. As shown in Figure 5a, the O_GM and O_GA electrodes show quite similar CV curves with a prominent cathodic peak at ~0.5−0.9 V in the first cycle, which is assigned to the decomposition of electrolyte associated with the formation of solid electrolyte interphase (SEI) on the surface of electrodes.[39,40] Note that the O_GM electrode exhibits a few weak redox peaks in the first cycle, (e.g., cathodic peaks at 1.3, 1.6, and 2.0 V, anodic peaks at 1.9 and 2.4 V), presumably resulting from the irreversible electrochemical lithiation and delithiation processes on the defect sites.[41] From the second cycle onward, the CV curves of the electrodes nearly overlapped, implying the good reversible and stable electrochemical reactions on the electrodes. Further galvanostatic charge−discharge measurements were used to estimate the cycling performance the O_GM and O_GA electrodes for
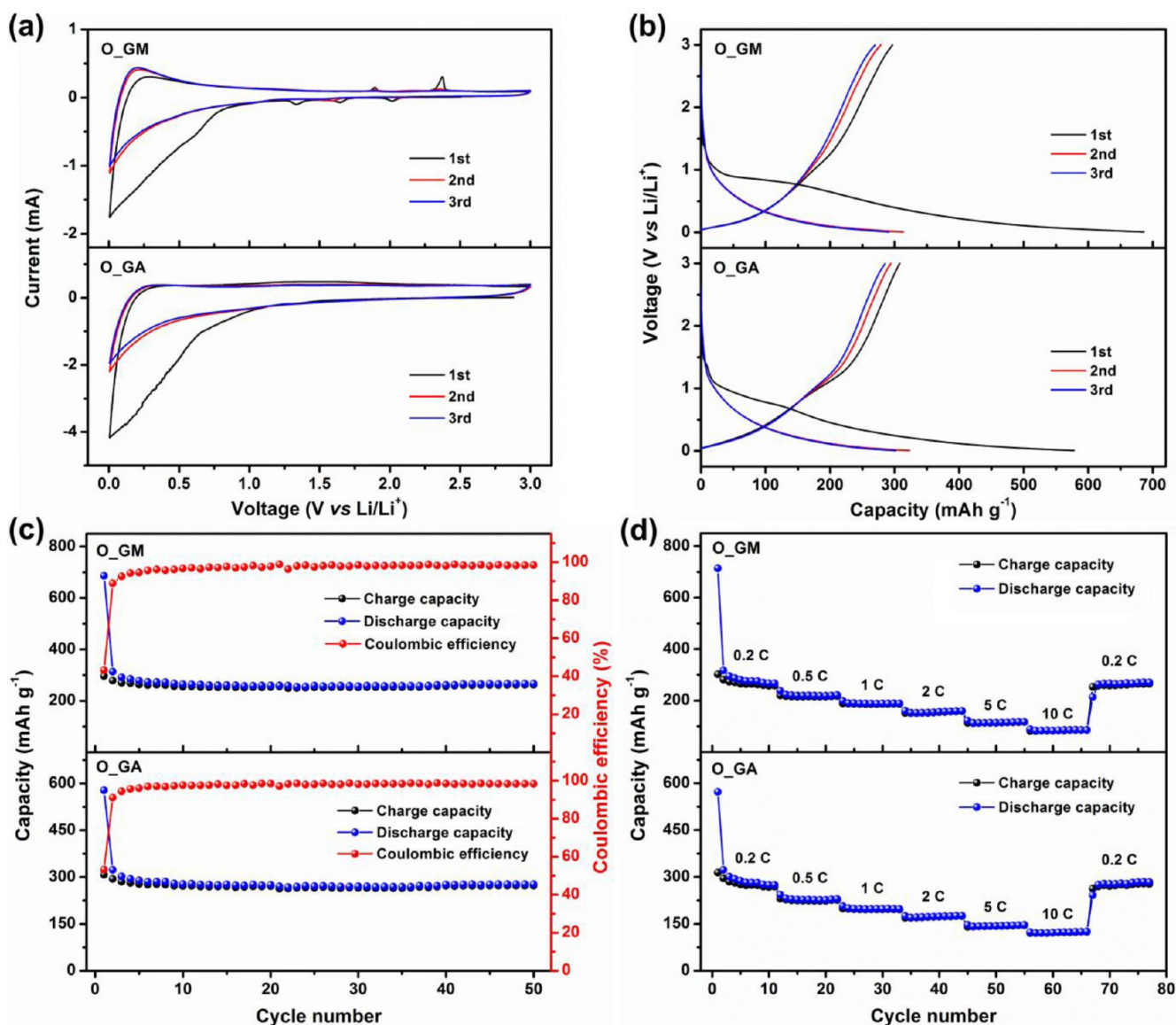
Figure 5. (a) Initial three CV curves of the O_GA and O_GM electrodes at a scanning rate of 0.5 mV s^{-1}. (b) Charge−discharge profiles of the O_GA and O_GM electrodes in the first three cycles. (c) Cycling performance the O_GA and O_GM electrodes measured between 0.005 and 3.0 V at a current rate of 0.2 C. (d) Rate capability of the O_GA and O_GM electrodes at programmed C rates ranging from 0.2 to 10 C.

LIBs. Figure 5b shows the initial three charge−discharge profiles of the O_GM and O_GA electrodes measured between 0.005 and 3.0 V at a current rate of 0.2 C (1 C = 372 mA g^{-1}). Clearly, a sloping plateau at ∼0.8 V is observed in the first discharge curve but disappears in the subsequent cycles, indicative of SEI formation on the electrode, which matches well with the CV curves in Figure 5a.[42] The first discharge capacity of O_GM is calculated to be 686 mAh g^{-1}, much larger than that of O_GA electrode (578 mAh g^{-1}). The increased Li storage capacity in O_GM mainly originates from its defect-enriched structure that is beneficial for further Li accommodation. However, after the first cycle, the capacities of O_GM and O_GA electrodes suddenly drop to ∼300 mAh g^{-1} in the following 50 cycles (Figure 5c). Moreover, the rate capacities of O_GM are also comparable to O_GA except for the first cycle, as shown in Figure 5d and Figure S2. This interesting phenomenon likely results from the stacked structure in the electrode materials. As shown in the aforementioned discussions, both O_GM and O_GA are

consisted by graphene aggregations with low BET surface areas and porosity, which result in limited accessibility to the electrolyte and slow mass transport. Therefore, only the outer-surface regions of the electrode materials can contribute to the final Li storage capacities.

Upon oven drying, the removal of water within the graphene sheets will induce a severe restacking of graphene sheets, thus leading to a low BET surface area with the collapse of pores, even though a portion of micropores and mesopores survived. Fortunately, these issues can be resolved, or at least minimized, using the freeze-drying technique. As shown in Figure 6a−d, the FESEM images of F_GA and F_GM exhibit a loose-packed structure with crumpled graphene sheets to form a porous structure. In particular, a mesh structure with densely distributed in-plane pores (∼60−200 nm) are clearly detected in F_GM (Figure 6c and 6d). Besides, some macropores with the pore sizes ranging from hundreds of nanometers to several micrometers are also observed in F_GM, which should be attributed to the accumulation of Fe_2O_3 nanoparticles that
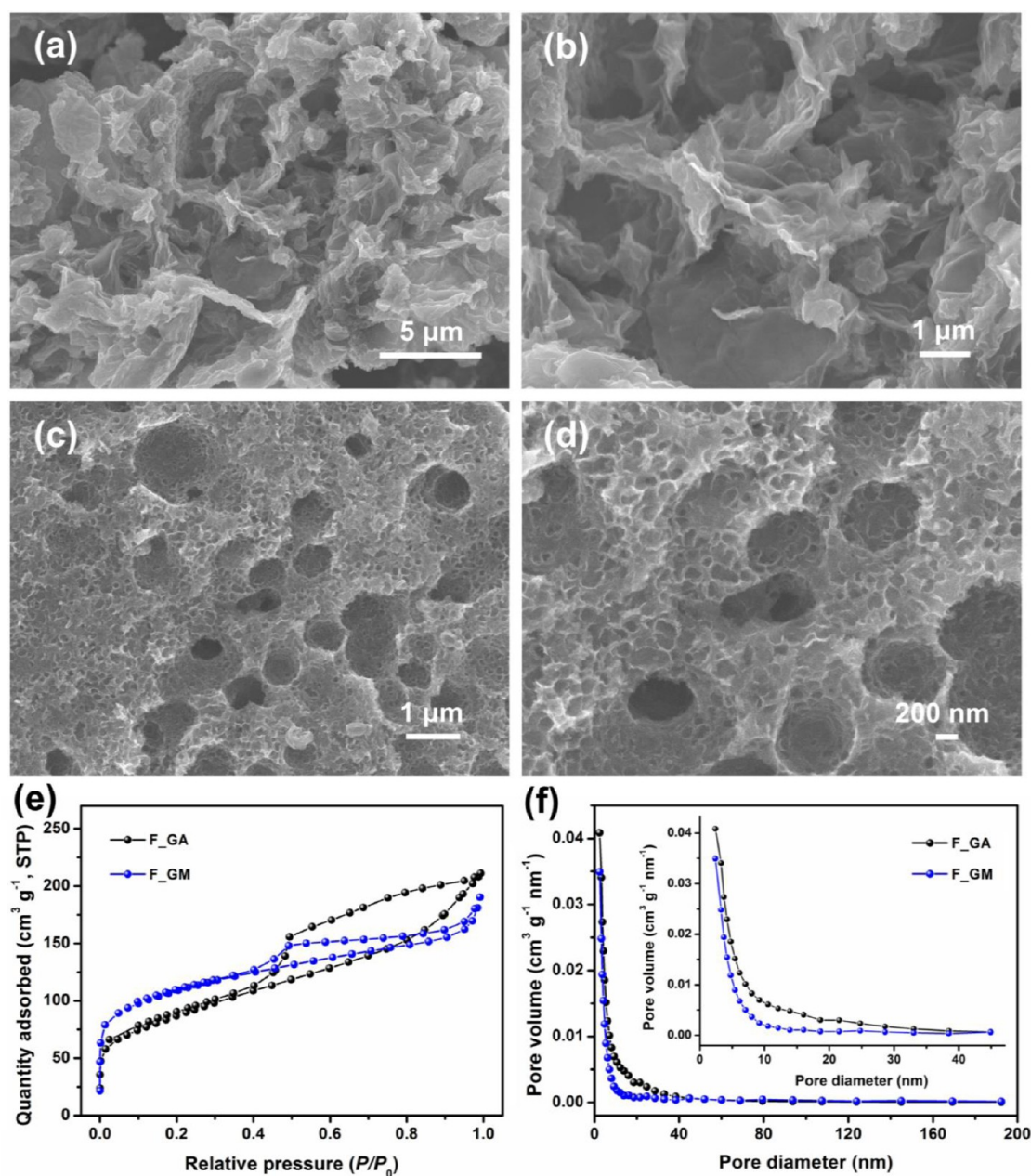
Figure 6. FESEM images of (a and b) F_GA and (c and d) F_GM. (e) N$_2$ adsorption−desorption isotherms and (f) the corresponding pore size distribution curves (inset: magnified 0−45 nm region) of F_GA and F_GM.

function as the porogen to facilitate the formation of pores in between the graphene sheets. In the Raman spectroscopy (Figure S3), the I_D/I_G ratio of F_GM (1.03) is a bit larger than that of F_GA (1.01), suggesting its more disordered structure caused by the in-plane holes induced defects or edges.[43,44] The BET calculation further demonstrates a surface area of 381 m^2 g^{-1} for F_GM and 311 m^2 g^{-1} for F_GA (Figure 6e), approximate 3-fold of these for O_GM and O_GA, verifying the effectiveness of freeze-drying in preventing the aggregation of graphene. Similar to O_GM and O_GA, F_GM and F_GA also present a wide distribution of pore sizes (Figure 6f). However, owing to the existence of numerous well-preserved micropores and mesopores, F_GM and F_GA show a relatively larger total pore volume and smaller average pore diameter in comparison with O_GM and O_GA (Table 1). It should be mentioned that these pores are advantages for LIBs, as

micropores can provide plenty of active sites for Li storage, while mesopores are beneficial for efficient mass transport.[45,46]

As expected, the F_GM and F_GA electrodes display improved electrochemical Li storage performances compared with the O_GM and O_GA electrodes. Specifically, the initial discharge capacity of F_GM and F_GA electrodes is 896 and 709 mAh g^{-1} at a current rate of 0.2 C (Figure 7a), respectively, much larger than the O_GM and O_GA electrodes, documenting the pore structure plays an important role in LIBs. Moreover, the capacity of F_GM electrode is always larger than that of F_GA within the 300 continuous cycles (Figure 7b). Note that both electrodes show a slight capacity reduction in the first few cycles and then a capacity increase upon cycling, which is commonly observed in graphene-based anodes.[9,15] The origin of this interesting phenomenon could be ascribed to the delayed accessibility of Li ions into the inner
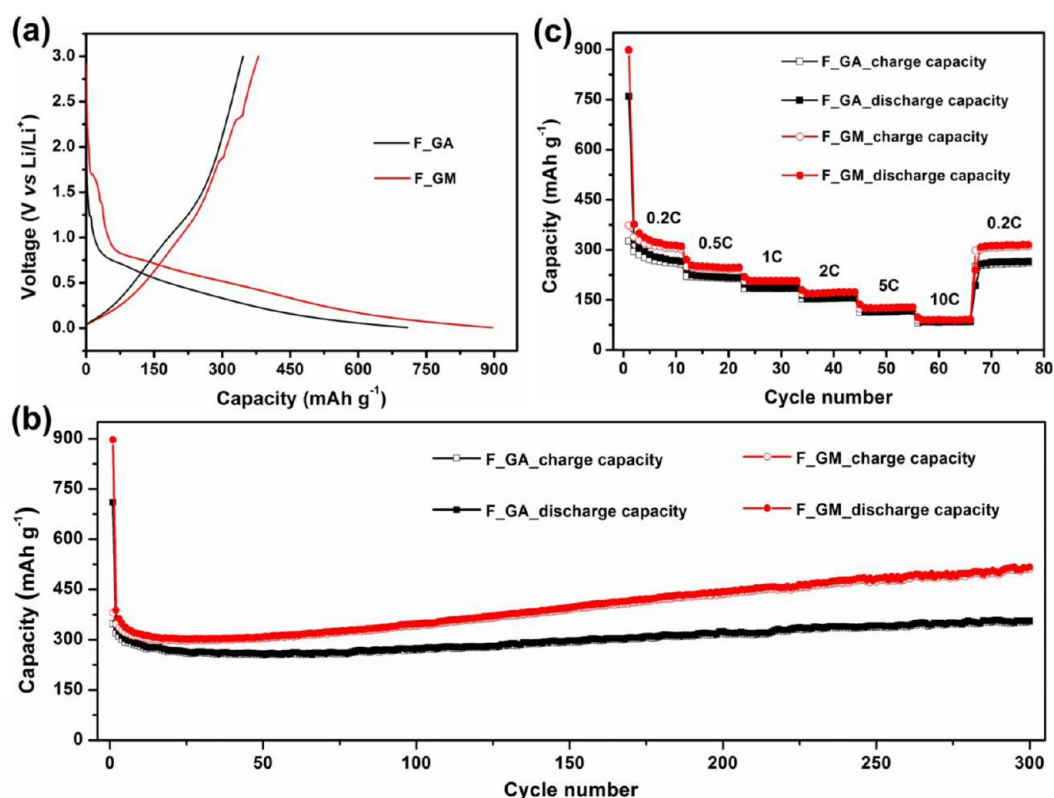
Figure 7. (a) Initial charge−discharge profiles of the F_GA and F_GM electrodes measured between 0.005 and 3.0 V. (b) Cycling performance the F_GA and F_GM electrodes at a current rate of 0.2 C. (c) Rate capability of the F_GA and F_GM electrodes at various C rates.
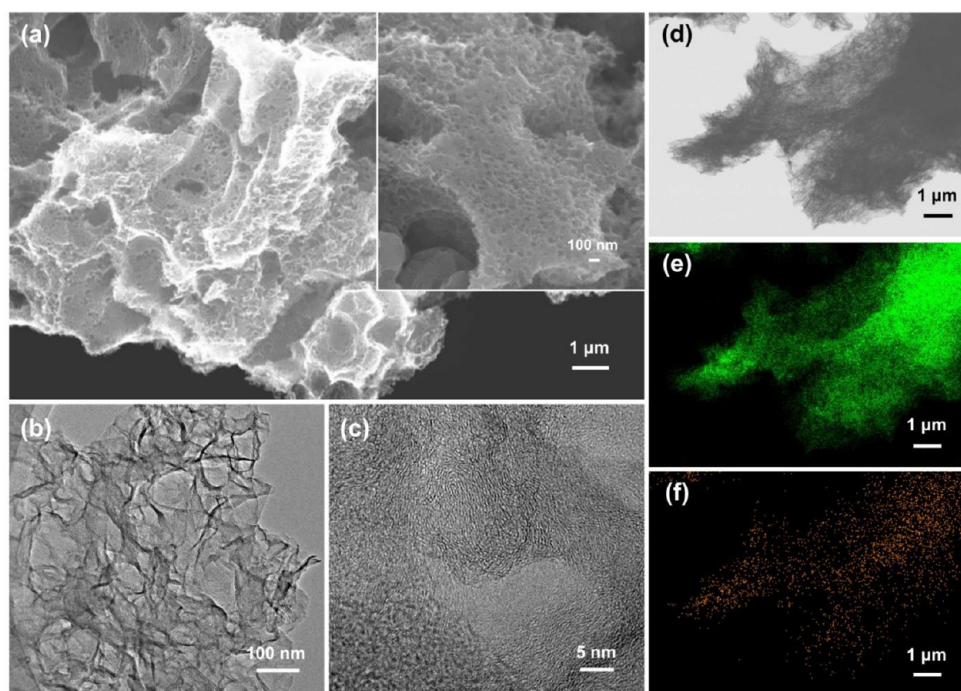

Figure 8. (a) FESEM image of NGM. Inset: Corresponding higher-magnification FESEM image. (b) TEM and (c) HRTEM images of NGM. (d) Bright-field STEM image of NGM and the corresponding EDS elemental mapping images of (e) carbon (green) and (f) nitrogen (brown).

part of the electrode. The F_GM electrode still delivers a capacity of 516 mAh g^{-1} after 300 cycles, which is 1.4 times that of F_GA (356 mAh g^{-1}). Additionally, the electrode of F_GM also holds a good rate capability. As shown in Figure 7c and Figure S4, the F_GM electrode is capable of delivering a

capacity of 313, 246, 208, 172, 125, and 90 mA h g^{-1} at the current rate of 0.2, 0.5, 1, 2, 5, and 10 C, respectively. All these values are larger than those of F_GA electrode, proving the critical role of defects in improving the Li storage performances of graphene.
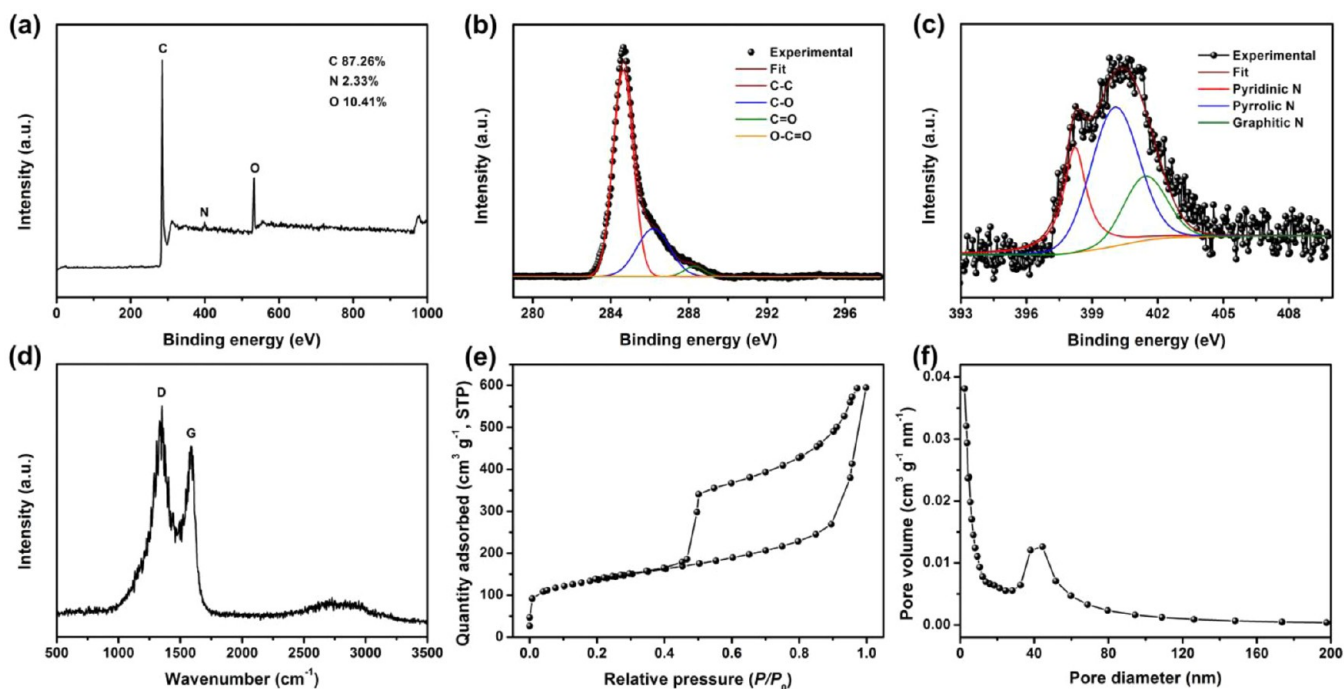
Figure 9. Structural characterization of NGM. (a) XPS survey spectrum, (b) high-resolution C 1s and (c) N 1s XPS spectra of NGM. (d) Raman spectrum of NGM. (e) N_2 adsorption−desorption isotherms and (f) the corresponding pore size distribution curves of NGM.
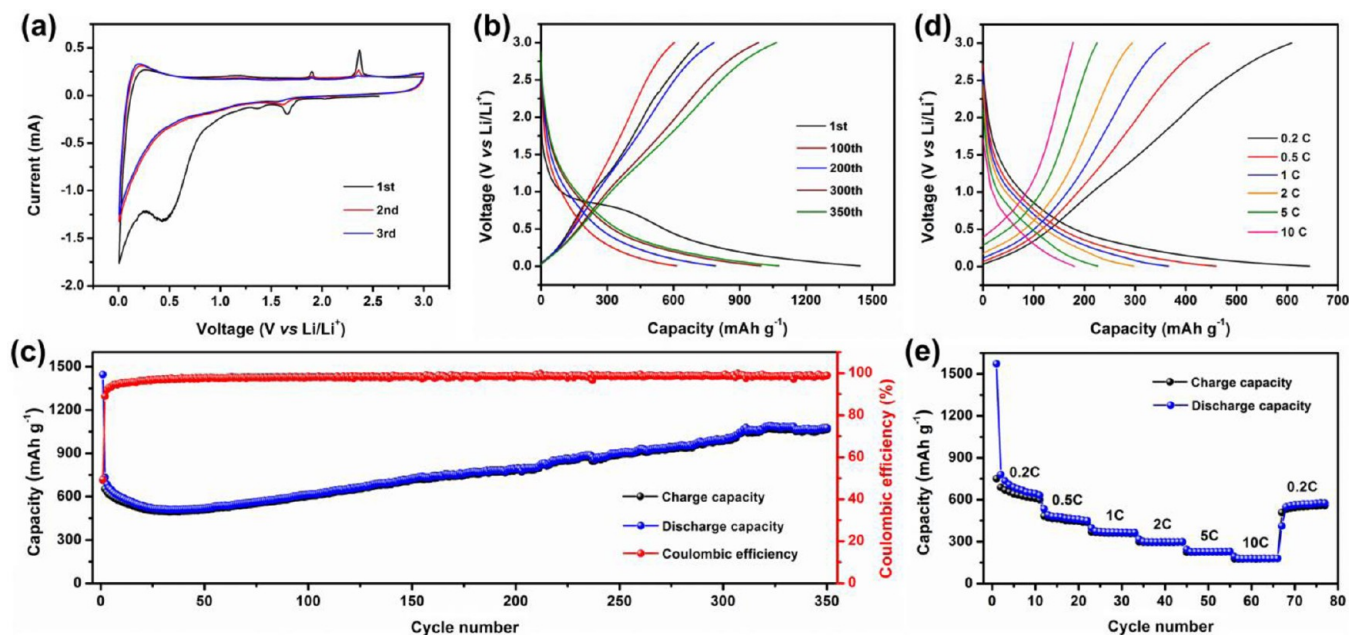

Figure 10. (a) CV curves of the NGM electrode at a scanning rate of 0.5 mV s^{-1}. (b) Charge−discharge profiles and (c) cycling performance of the NGM electrode measured between 0.005 and 3.0 V at a current rate of 0.2 C. (d) Charge−discharge profiles and (e) rate capability of the NGM electrode at programmed C rates ranging from 0.2 to 10 C.

To further upgrade the electrochemical performances, we have fabricated NGM using urea as the nitrogen source. Figure 8 shows morphological characterizations of NGM. Similar to F_GM, the FESEM images of NGM (Figure 8a) exhibit a porous structure with abundant in-plane poles. TEM image (Figure 8b) reveals that NGM has an interconnected porous network consisted by the randomly distributed graphene thin layers with etched holes. HRTEM image of NGM (Figure 8c) manifests short-range order of lattice structures due to the interrupted sp^2-bonding networks, by reason for oxidation induced sp^3 bonds.[47] In addition, a typical hole with a size of ∼5 × 15 nm can also observed in Figure 8c. The bright-field scanning transmission electron microscopy (STEM) image of NGM (Figure 8d) and the corresponding energy dispersive X-ray spectroscopy (EDS) elemental mapping (Figure 8e and 8f) disclose the homogeneous distribution of nitrogen over the entire graphene mesh.

Figure 9a-c show the XPS measurements of NGM. Except for C 1s and O 1s peaks, the appearance of a pronounced peak located at ~400 eV in the XPS survey spectrum (Figure 9a) verifies the successful incorporation of N into the graphene networks, which is well consistent with the EDS analysis (Figure 8f).[48] The N doping content is calculated to be 2.33%. Besides, NGM also exhibits an extremely decreased O content (Figure 9a and 9b) as compared to GO (Figure 3a), indicative of the efficient removal of oxygen-related functional groups. The high-resolution N 1s XPS spectrum of NGM (Figure 9c) presents three peaks of 398.2, 400.0, and 401.4 eV, corresponding to the pyridinic N, pyrrolic N and graphitic N, respectively.[9,49] It can be seen that pyridinic N and pyrrolic N are the two main components in NGM (Table S1), both of which are favorable for Li storage according to the theoretical results.[50,51] Raman spectrum of NGM (Figure 9d) illustrates a large I_D/I_G ratio of 1.1 due to the emergence of substantial defects evoked by the in-plane holes and N doping. The N_2 adsorption−desorption isotherms (Figure 9e) show a classic IV pattern with a steep uptake at low pressure ($P/P_0 < 0.01$) and a clear hysteresis loops at $P/P_0 = 0.5-1.0$, which signifies the coexistence of micropores and mesopores within the NGM.[52] The BET surface area of NGM reaches up to 487 m² g⁻¹ with a total pore volume of 0.86 cm³ g⁻¹. The pore size distribution curve of NGM (Figure 9f) confirms its multimodel pore structures with both micropores peaked at 2.0 nm and mesopores peaked at 41 nm. Such an appealing porous texture not only benefits for the infiltration of electrolyte, but also facilitates the accessibility of Li ions to the entire electrode.

The CV curves of NGM (Figure 10a) shows a similar feature with that of F_GM (Figure S5) and O_GM (Figure 5a), except for the higher redox current peaks, because of its more disordered structure with massive defects. However, the NGM electrode exhibits significantly improved electrochemical performances with respect to the other electrodes. As shown in Figure 10b and 10c, the NGM electrode delivers initial discharge and charge capacities of 1444 and 713 mAh g⁻¹, respectively, corresponding to a Coulombic efficiency of 49.4%. The capacity loss can be assigned to the following two reasons: (i) the irreversible electrochemical processes proceed on the defect sites; (ii) the decomposition of electrolyte associated with SEI formation on the electrode. With continuous cycling, the electrochemical reactions progressively become reversible, leading to a rapid increase of Coulombic efficiency, for example, 89% in the second cycle and 92% in the third cycle. It can be seen that a stable capacity of 1078 mAh g⁻¹ can still be obtained after 350 cycles, nearly three times that of the theoretical value of the commercialized graphite (372 mAh g⁻¹) and also higher than the recently reported graphene-based anodes.[41,53,54] Figure 10d and 10e show the rate performance of NGM electrode tested at programmed C rates. Along with the current density increases from 0.2 to 10 C, the electrode is capable of delivering stabilized capacities of 644, 460, 366, 298, 227, and 180 mAh g⁻¹, respectively. Particularly, even when the current density suddenly jumps from 10 to 0.2 C, a reversible capacity of 578 mAh g⁻¹ could be still recovered. These results are definitely superior to the GMs and GAs anodes. The prominent electrochemical performances are mainly attributed to the synergistic effects between defects (in-plane holes and N doping) and pores structure. On one hand, the presence of in-plane holes and N doping in the graphene sheets induce plentiful topological defects, which could act as the active sites for additional Li storage. Moreover, the doped N atoms is also

able to increase the conductivity of the electrode, thus leading to a low charge transfer resistance. As shown in Figure S6, the NGM electrode exhibits a lower charge transfer resistance (66 Ω) in comparison with the F_GM (101 Ω) and O_GM (114 Ω) electrodes. On the other hand, the large BET surface area and total pore volume of NGM not only provide huge and sufficient accessible areas for electrolyte, but also ensure fast and efficient Li diffusion. Specifically, the micropores and small mesopores can serve as the "cavities" for further Li accommodation.

CONCLUSIONS

In summary, we have developed a facile and effective approach to fabricate GM with a densely distributed in-plane pores of ~60−200 nm by Fe_2O_3 nanoparticles-assisted etching process. The anodic performance of GMs with different porosities in comparison with GAs is systematically investigated, which reveals that only when merged with adequate porous structure, the GMs electrodes can exhibit better electrochemical performances than GAs. The performance of GM can be upgraded through further N doping by using urea as the source of nitrogen. The as-obtained NGM possesses appropriate porous structure, N doping content, and abundant in-plane pores, thus leading to high Li storage capacity with long cyclic life (1078 mAh g⁻¹ after 350 cycles at 0.2 C) and outstanding rate performance of 180 mAh g⁻¹ at 10 C. This work discloses the vital role of defects and pore structure in the anodic performance of graphene, which is probably useful for constructing advanced graphene-based materials for diverse applications, particularly in electrochemical fields.

ASSOCIATED CONTENT

Ⓢ Supporting Information

The Supporting Information is available free of charge on the ACS Publications website at DOI: 10.1021/acsami.6b12319.

> FESEM images of G@Fe₂O₃, charge−discharge profiles of the O_GA and O_GM electrodes at programmed C rates, Raman spectra of F_GA and F_GM, charge−discharge profiles of the F_GA and F_GM electrodes at programmed C rates, CV curves of the F_GA and F_GM electrodes, Nyquist plots of the NGM, F_GM, and O_GM electrodes, and the atomic percentage of N species in NGM (PDF)

AUTHOR INFORMATION

Corresponding Authors
*E-mail: iamjqliu@njtech.edu.cn.
*E-mail: yuting@ntu.edu.sg.
*E-mail: iamwhuang@njtech.edu.cn.
ORCID Ⓘ
Wei Huang: 0000-0001-7004-6408

Notes
The authors declare no competing financial interest.

ACKNOWLEDGMENTS

■ REFERENCES

(1) Chen, K.; Song, S.; Liu, F.; Xue, D. Structural Design of Graphene for Use in Electrochemical Energy Storage Devices. *Chem. Soc. Rev.* **2015**, *44*, 6230−6257.

(2) Ai, W.; Zhou, W.; Du, Z.; Sun, C.; Yang, J.; Chen, Y.; Sun, Z.; Feng, S.; Zhao, J.; Dong, X.; Huang, W.; Yu, T. Toward High Energy Organic Cathodes for Li-Ion Batteries: A Case Study of Vat Dye/Graphene Composites. *Adv. Funct. Mater.* **2016**, DOI: 10.1002/adfm.201603603.

(3) Raccichini, R.; Varzi, A.; Passerini, S.; Scrosati, B. The Role of Graphene for Electrochemical Energy Storage. *Nat. Mater.* **2015**, *14*, 271−279.

(4) Wang, G.; Shen, X.; Yao, J.; Park, J. Graphene Nanosheets for Enhanced Lithium Storage in Lithium Ion Batteries. *Carbon* **2009**, *47*, 2049−2053.

(5) Ai, W.; Zhu, J. H.; Jiang, J.; Chao, D. L.; Wang, Y. L.; Ng, C. F.; Wang, X. L.; Wu, C.; Li, C. M.; Shen, Z. X.; Huang, W.; Yu, T. Surfactant-Assisted Encapsulation of Uniform SnO_2 Nanoparticles in Graphene Layers for High-Performance Li-Storage. *2D Mater.* **2015**, *2*, 014005.

(6) Yoo, E.; Kim, J.; Hosono, E.; Zhou, H. S.; Kudo, T.; Honma, I. Large Reversible Li Storage of Graphene Nanosheet Families for Use in Rechargeable Lithium Ion Batteries. *Nano Lett.* **2008**, *8*, 2277−2282.

(7) Yin, S.; Zhang, Y.; Kong, J.; Zou, C.; Li, C. M.; Lu, X.; Ma, J.; Boey, F. Y. C.; Chen, X. Assembly of Graphene Sheets into Hierarchical Structures for High-Performance Energy Storage. *ACS Nano* **2011**, *5*, 3831−3838.

(8) Wang, Z. L.; Xu, D.; Wang, H. G.; Wu, Z.; Zhang, X. B. In Situ Fabrication of Porous Graphene Electrodes for High-Performance Energy Storage. *ACS Nano* **2013**, *7*, 2422−2430.

(9) Ai, W.; Jiang, J.; Zhu, J.; Fan, Z.; Wang, Y.; Zhang, H.; Huang, W.; Yu, T. Supramolecular Polymerization Promoted in Situ Fabrication of Nitrogen-Doped Porous Graphene Sheets as Anode Materials for Li-Ion Batteries. *Adv. Energy Mater.* **2015**, *5*, 1500559.

(10) Leggesse, E. G.; Chen, C. L.; Jiang, J. C. Lithium Diffusion in Graphene and Graphite: Effect of Edge Morphology. *Carbon* **2016**, *103*, 209−216.

(11) Persson, K.; Sethuraman, V. A.; Hardwick, L. J.; Hinuma, Y.; Meng, Y. S.; van der Ven, A.; Srinivasan, V.; Kostecki, R.; Ceder, G. Lithium Diffusion in Graphitic Carbon. *J. Phys. Chem. Lett.* **2010**, *1*, 1176−1180.

(12) Han, X.; Funk, M. R.; Shen, F.; Chen, Y. C.; Li, Y.; Campbell, C. J.; Dai, J.; Yang, X.; Kim, J. W.; Liao, Y.; Connell, J. W.; Barone, V.; Chen, Z.; Lin, Y.; Hu, L. Scalable Holey Graphene Synthesis and Dense Electrode Fabrication Toward High-Performance Ultracapacitors. *ACS Nano* **2014**, *8*, 8255−8265.

(13) Peng, Y. Y.; Liu, Y.-M.; Chang, J. K.; Wu, C. H.; Ger, M. D.; Pu, N. W.; Chang, C. L. A Facile Approach to Produce Holey Graphene and Its Application in Supercapacitors. *Carbon* **2015**, *81*, 347−356.

(14) Wang, X.; Lv, L.; Cheng, Z.; Gao, J.; Dong, L.; Hu, C.; Qu, L. High-Density Monolith of N-Doped Holey Graphene for Ultrahigh Volumetric Capacity of Li-Ion Batteries. *Adv. Energy Mater.* **2016**, *6*, 1502100.

(15) Ai, W.; Luo, Z.; Jiang, J.; Zhu, J.; Du, Z.; Fan, Z.; Xie, L.; Zhang, H.; Huang, W.; Yu, T. Nitrogen and Sulfur Codoped Graphene: Multifunctional Electrode Materials for High-Performance Li-Ion

Batteries and Oxygen Reduction Reaction. *Adv. Mater.* **2014**, *26*, 6186−6192.

(16) Ma, X.; Ning, G.; Qi, C.; Xu, C.; Gao, J. Phosphorus and Nitrogen Dual-Doped Few-Layered Porous Graphene: A High-Performance Anode Material for Lithium-Ion Batteries. *ACS Appl. Mater. Interfaces* **2014**, *6*, 14415−14422.

(17) Ning, G.; Xu, C.; Cao, Y.; Zhu, X.; Jiang, Z.; Fan, Z.; Qian, W.; Wei, F.; Gao, J. Chemical Vapor Deposition Derived Flexible Graphene Paper and Its Application as High Performance Anodes for Lithium Rechargeable Batteries. *J. Mater. Chem. A* **2013**, *1*, 408−414.

(18) Jiang, Z.; Pei, B.; Manthiram, A. Randomly Stacked Holey Graphene Anodes for Lithium Ion Batteries with Enhanced Electrochemical Performance. *J. Mater. Chem. A* **2013**, *1*, 7775−7781.

(19) Sun, J.; Wang, L.; Song, R.; Yang, S. Nitrogen-Doped Holey Graphene Foams for High-Performance Lithium Storage. *RSC Adv.* **2015**, *5*, 91114−91119.

(20) Zhao, X.; Hayner, C. M.; Kung, M. C.; Kung, H. H. Flexible Holey Graphene Paper Electrodes with Enhanced Rate Capability for Energy Storage Applications. *ACS Nano* **2011**, *5*, 8739−8749.

(21) Zuo, Z.; Kim, T. Y.; Kholmanov, I.; Li, H.; Chou, H.; Li, Y. Ultra-Light Hierarchical Graphene Electrode for Binder-Free Supercapacitors and Lithium-Ion Battery Anodes. *Small* **2015**, *11*, 4922−4930.

(22) Cao, H.; Zhou, X.; Zheng, C.; Liu, Z. Metal Etching Method for Preparing Porous Graphene as High Performance Anode Material for Lithium-Ion Batteries. *Carbon* **2015**, *89*, 41−46.

(23) Zhang, J.; Guo, B.; Yang, Y.; Shen, W.; Wang, Y.; Zhou, X.; Wu, H.; Guo, S. Large Scale Production of Nanoporous Graphene Sheets and Their Application in Lithium Ion Battery. *Carbon* **2015**, *84*, 469−478.

(24) Xu, J.; Lin, Y.; Connell, J. W.; Dai, L. Nitrogen-Doped Holey Graphene as an Anode for Lithium-Ion Batteries with High Volumetric Energy Density and Long Cycle Life. *Small* **2015**, *11*, 6179−6185.

(25) Ren, W.; Cheng, H. M. The Global Growth of Graphene. *Nat. Nanotechnol.* **2014**, *9*, 726−730.

(26) Ai, W.; Zhou, W.; Du, Z.; Du, Y.; Zhang, H.; Jia, X.; Xie, L.; Yi, M.; Yu, T.; Huang, W. Benzoxazole and Benzimidazole Heterocycle-Grafted Graphene for High-Performance Supercapacitor Electrodes. *J. Mater. Chem.* **2012**, *22*, 23439−23446.

(27) Palaniselvam, T.; Aiyappa, H. B.; Kurungot, S. An Efficient Oxygen Reduction Electrocatalyst from Graphene by Simultaneously Generating Pores and Nitrogen Doped Active Sites. *J. Mater. Chem.* **2012**, *22*, 23799−23805.

(28) Liu, D. H.; Lu, H. Y.; Wu, X. L.; Wang, J.; Yan, X.; Zhang, J. P.; Geng, H.; Zhang, Y.; Yan, Q. A New Strategy for Developing Superior Electrode Materials for Advanced Batteries: Using a Positive Cycling Trend to Compensate the Negative One to Achieve Ultralong Cycling Stability. *Nanoscale Horiz.* **2016**, *1*, 496−501.

(29) Liu, D. H.; Li, W.; Wan, F.; Fan, C. Y.; Wang, Y. Y.; Zhang, L. L.; Lu, H. Y.; Xing, Y. M.; Zhang, X. H.; Wu, X. L. Restraining Capacity Increase to Achieve Ultrastable Lithium Storage: Case Study of a Manganese(II) Oxide/Graphene-Based Nanohybrid and Its Full-Cell Performance. *ChemElectroChem* **2016**, *3*, 1354−1359.

(30) Wang, J.; Ding, B.; Hao, X.; Xu, Y.; Wang, Y.; Shen, L.; Dou, H.; Zhang, X. A Modified Molten-Salt Method to Prepare Graphene Electrode with High Capacitance and Low Self-Discharge Rate. *Carbon* **2016**, *102*, 255−261.

(31) Liu, D. H.; Lu, H. Y.; Wu, X. L.; Hou, B. H.; Wan, F.; Bao, S. D.; Yan, Q.; Xie, H. M.; Wang, R. S. Constructing the Optimal Conductive Network in MnO-Based Nanohybrids as High-Rate and Long-Life Anode Materials for Lithium-Ion Batteries. *J. Mater. Chem. A* **2015**, *3*, 19738−19746.

(32) Du, Z.; Ai, W.; Xie, L.; Huang, W. Organic Radical Functionalized Graphene As a Superior Anode Material for Lithium-Ion Batteries. *J. Mater. Chem. A* **2014**, *2*, 9164−9168.

(33) Ai, W.; Du, Z.; Fan, Z.; Jiang, J.; Wang, Y.; Zhang, H.; Xie, L.; Huang, W.; Yu, T. Chemically Engineered Graphene Oxide as High

Performance Cathode Materials for Li-Ion Batteries. *Carbon* **2014**, *76*, 148−154.

(34) Yu, B. Y.; Kwak, S. Y. Assembly of Magnetite Nanocrystals into Spherical Mesoporous Aggregates with a 3-D Wormhole-Like Pore Structure. *J. Mater. Chem.* **2010**, *20*, 8320−8328.

(35) Pei, S.; Cheng, H. M. The Reduction of Graphene Oxide. *Carbon* **2012**, *50*, 3210−3228.

(36) Ai, W.; Cao, X.; Sun, Z.; Jiang, J.; Du, Z.; Xie, L.; Wang, Y.; Wang, X.; Zhang, H.; Huang, W.; Yu, T. Redox-Crosslinked Graphene Networks with Enhanced Electrochemical Capacitance. *J. Mater. Chem. A* **2014**, *2*, 12924−12930.

(37) Sun, L.; Fu, Y.; Tian, C.; Yang, Y.; Wang, L.; Yin, J.; Ma, J.; Wang, R.; Fu, H. Isolated Boron and Nitrogen Sites on Porous Graphitic Carbon Synthesized from Nitrogen-Containing Chitosan for Supercapacitors. *ChemSusChem* **2014**, *7*, 1637−1646.

(38) Zhang, L.; Shi, G. Preparation of Highly Conductive Graphene Hydrogels for Fabricating Supercapacitors with High Rate Capability. *J. Phys. Chem. C* **2011**, *115*, 17206−17212.

(39) Goh, B. M.; Wang, Y.; Reddy, M. V.; Ding, Y. L.; Lu, L.; Bunker, C.; Loh, K. P. Filling the Voids of Graphene Foam with Graphene "Eggshell" for Improved Lithium-Ion Storage. *ACS Appl. Mater. Interfaces* **2014**, *6*, 9835−9841.

(40) Sui, Z. Y.; Wang, C.; Yang, Q. S.; Shu, K.; Liu, Y. W.; Han, B. H.; Wallace, G. G. A Highly Nitrogen-Doped Porous Graphene - An Anode Material for Lithium Ion Batteries. *J. Mater. Chem. A* **2015**, *3*, 18229−18237.

(41) Wang, X.; Ai, W.; Li, N.; Yu, T.; Chen, P. Graphene-Bacteria Composite for Oxygen Reduction and Lithium Ion Batteries. *J. Mater. Chem. A* **2015**, *3*, 12873−12879.

(42) Wang, H. G.; Wang, Y.; Li, Y.; Wan, Y.; Duan, Q. Exceptional Electrochemical Performance of Nitrogen-doped Porous Carbon for Lithium Storage. *Carbon* **2015**, *82*, 116−123.

(43) Zuo, Z.; Kim, T. Y.; Kholmanov, I.; Li, H.; Chou, H.; Li, Y. Ultra-Light Hierarchical Graphene Electrode for Binder-Free Supercapacitors and Lithium-Ion Battery Anodes. *Small* **2015**, *11*, 4922−4930.

(44) Masarapu, C.; Subramanian, V.; Zhu, H.; Wei, B. Long-Cycle Electrochemical Behavior of Multiwall Carbon Nanotubes Synthesized on Stainless Steel in Li Ion Batteries. *Adv. Funct. Mater.* **2009**, *19*, 1008−1014.

(45) Zheng, Z.; Zhang, X.; Pei, F.; Dai, Y.; Fang, X.; Wang, T.; Zheng, N. Hierarchical Porous Carbon Microrods Composed of Vertically Aligned Graphene-Like Nanosheets for Li-Ion Batteries. *J. Mater. Chem. A* **2015**, *3*, 19800−19806.

(46) Zhao, D.; Wang, L.; Yu, P.; Zhao, L.; Tian, C.; Zhou, W.; Zhang, L.; Fu, H. From Graphite to Porous Graphene-Like Nanosheets for High Rate Lithium-Ion Batteries. *Nano Res.* **2015**, *8*, 2998−3010.

(47) Ai, W.; Zhou, W.; Du, Z.; Chen, Y.; Sun, Z.; Wu, C.; Zou, C.; Li, C.; Huang, W.; Yu, T. Nitrogen and Phosphorus Codoped Hierarchically Porous Carbon as an Efficient Sulfur Host for Li-S Batteries. *Energy Storage Mater.* **2017**, *6*, 112−118.

(48) Tian, L. L.; Li, S. B.; Zhang, M. J.; Li, S. K.; Lin, L. P.; Zheng, J. X.; Zhuang, Q. C.; Amine, K.; Pan, F. Cascading Boost Effect on the Capacity of Nitrogen-Doped Graphene Sheets for Li- and Na-Ion Batteries. *ACS Appl. Mater. Interfaces* **2016**, *8*, 26722−26729.

(49) Jiang, Z.; Jiang, Z. J.; Tian, X.; Luo, L. Nitrogen-doped Graphene Hollow Microspheres as an Efficient Electrode Material for Lithium Ion Batteries. *Electrochim. Acta* **2014**, *146*, 455−463.

(50) Ma, C.; Shao, X.; Cao, D. Nitrogen-Doped Graphene Nanosheets as Anode Materials for Lithium Ion Batteries: a First-Principles Study. *J. Mater. Chem.* **2012**, *22*, 8911−8915.

(51) Hardikar, R. P.; Das, D.; Han, S. S.; Lee, K. R.; Singh, A. K. Boron Doped Defective Graphene as a Potential Anode Material for Li-Ion Batteries. *Phys. Chem. Chem. Phys.* **2014**, *16*, 16502−16508.

(52) Chen, L. F.; Zhang, X. D.; Liang, H. W.; Kong, M.; Guan, Q. F.; Chen, P.; Wu, Z. Y.; Yu, S. H. Synthesis of Nitrogen-Doped Porous Carbon Nanofibers as an Efficient Electrode Material for Supercapacitors. *ACS Nano* **2012**, *6*, 7092−7102.

(53) Zhang, X.; Han, S.; Xiao, P.; Fan, C.; Zhang, W. Thermal Reduction of Graphene Oxide Mixed with Hard Carbon and Their High Performance as Lithium Ion Battery Anode. *Carbon* **2016**, *100*, 600−607.

(54) Zhang, X.; Fan, C.; Li, L.; Zhang, W.; Zeng, W.; He, X.; Han, S. Hard Carbon Wrapped in Graphene Networks as Lithium Ion Battery Anode. *Electrochim. Acta* **2014**, *149*, 94−100.